Journal of Neural Engineering

PAPER

Quantitative simulation of extracellular single unit recording from the surface of cortex

To cite this article: Mackenna Hill *et al* 2018 *J. Neural Eng.* **15** 056007

IOP Publishing | Journal of Neural Engineering

J. Neural Eng. **15** (2018) 056007 (12pp) https://doi.org/10.1088/1741-2552/aacdb8

Quantitative simulation of extracellular single unit recording from the surface of cortex

Mackenna Hill[1,2,11], Estefania Rios[1,11], Shyam Kumar Sudhakar[3], Douglas H Roossien[4], Ciara Caldwell[1], Dawen Cai[4,5,6], Omar J Ahmed[3], Scott F Lempka[1,7] and Cynthia A Chestek[1,8,9,10]

[1] Department of Biomedical Engineering, University of Michigan, Ann Arbor, MI, United State of America
[2] Department of Biomedical Engineering, Duke University, Durham, NC, United State of America
[3] Department of Psychology, University of Michigan, Ann Arbor, MI, United State of America
[4] Department of Cell and Developmental Biology, University of Michigan, Ann Arbor, Michigan, United State of America
[5] Neuroscience Graduate Program of the Medical School, University of Michigan, Ann Arbor, MI, United State of America
[6] Department of Biophysics of LS&A, University of Michigan, Ann Arbor, MI, United State of America
[7] Biointerfaces Institute, University of Michigan, Ann Arbor, MI, United State of America
[8] Department of Electrical Engineering and Computer Science, University of Michigan, Ann Arbor, MI, United States of America
[9] Neurosciences Program, University of Michigan, Ann Arbor, MI, United States of America
[10] Robotics Program, University of Michigan, Ann Arbor, MI, United States of America

E-mail: cchesteck@umich.edu

Received 2 October 2017, revised 4 June 2018
Accepted for publication 20 June 2018
Published 11 July 2018

Abstract

Objective. Neural recording is important for a wide variety of clinical applications. Until recently, recording from the surface of the brain, even when using micro-electrocorticography (μECoG) arrays, was not thought to enable recording from individual neurons. Recent results suggest that when the surface electrode contact size is sufficiently small, it may be possible to record single neurons from the brain's surface. In this study, we use computational techniques to investigate the ability of surface electrodes to record the activity of single neurons. *Approach.* The computational model included the rat head, μECoG electrode, two existing multi-compartmental neuron models, and a novel multi-compartmental neuron model derived from patch clamp experiments in layer 1 of the cortex. *Main results.* Using these models, we reproduced single neuron recordings from μECoG arrays, and elucidated their possible source. The model resembles the experimental data when spikes originate from layer 1 neurons that are less than 60 μm from the cortical surface. We further used the model to explore the design space for surface electrodes. Although this model does not include biological or thermal noise, the results indicate the electrode contact area should be 100 μm^2 or smaller to maintain a detectable waveform amplitude. Furthermore, the model shows the width of lateral insulation could be reduced, which may reduce scar formation, while retaining 95% of signal amplitude. *Significance.* Overall, the model suggests single-unit surface recording is limited to neurons in layer 1 and further improvement in electrode design is needed.

Keywords: μECoG, electrocorticography, neural recording, brain–computer interfaces, computational model, computer simulation, microelectrodes

(Some figures may appear in colour only in the online journal)

[11] Authors contributed equally.

1. Introduction

Neurological diseases can significantly decrease the quality and duration of life. Neural recording electrodes are utilized as diagnostic tools and in therapeutic devices for a wide variety of conditions. Macroelectrode recording applications, such as invasive monitoring for epilepsy [1, 2] and local field potential recordings obtained from electrodes used in deep brain stimulation [3], use large surface area electrodes ($\sim$30 mm^2 to $\sim$0.3 mm^2) to record the activity of a large number of neurons within the brain. Microelectrode recording applications use small surface area electrodes ($\sim$1000 μm^2 to $\sim$10 μm^2) that can record the activity of single neurons. Microelectrodes are required for high resolution brain-machine interfaces (BMI) which are devices that aim to restore motor, sensory, and/or cognitive function [4–6].

Penetrating electrodes arrays have been used for decades in BMI applications. Common devices include the Utah array and the Michigan probe [7–9]. These types of electrodes have high spatial resolution and can record the activity of individual neurons (single units). However, all penetrating electrodes have limitations which prevent their widespread use, such as damage to the blood brain barrier, scarring from the foreign body reaction, and the inability to record from neurons greater than $\sim$100 μm from the electrode surface [10–14]. Recent advances in cellular-scale electrodes have mitigated some of these concerns [15, 16], but these novel arrays have lower channel counts and are not yet ready for clinical use.

Surface electrodes can address many of the limitations of penetrating electrodes. These electrodes are applied to the surface of the brain rather than being inserted into the brain. Thus, these surface electrodes do not disrupt the blood brain barrier. As a result, surface electrocorticography (ECoG) electrodes avoid brain damage and potentially increase long-term viability. However, ECoG electrodes have their own limitations. Because they present an impermeable solid surface to the brain, this may cause increased scarring over time [10, 17–19]. The primary limitation of ECoG electrodes is an increased distance between the electrodes and the neurons of interest. This distance decreases the selectivity of conventional ECoG electrodes so that they are only able to record ensemble activity [1, 20]. The inability to selectively record from small populations of neurons is logical because neural signals quickly fall off as function of distance from the electrode [11, 21].

Recently, one novel micro-electrocorticography (μECoG) grid was reported to overcome some of these limitations. Khodagholy *et al* 2015 [22] designed a μECoG grid (NeuroGrid), with much smaller electrode sizes than previous devices (100 μm^2), that was able to record signals at the brain surface that appear to be generated by single units in rats. Due to the clear advantages of surface recording, it is important to understand which type of neurons are being recorded, how deep these recordings extend, and the critical aspects of the electrode design that provide these unique capabilities.

The purpose of this study was to investigate these issues and the origin of the neural signals recorded with these μECoG surface microelectrodes using a computational modeling approach. Therefore, we built a computational model of surface recording, adapting the methods of Moffitt and McIntyre 2005 [11]. To our knowledge, this is the first neural recording model capable of replicating single-unit recording from the surface of the brain. First, we used two existing multi-compartmental cable models of pyramidal cells from layers 3 and 5 [23, 24] and developed a novel multi-compartment model that matched patch clamp data from layer 1 cells. Next, we developed finite element models (FEM) of electrodes with the NeuroGrid geometry along with several variants. Finally, we used a reciprocal solution approach to estimate the extracellular voltages that would be observed with recording electrodes of various sizes. We believe this model will help to determine the origin of single-unit recordings from μECoG electrode grids as well as potential technological improvements that can be made to optimize the recording fidelity.

2. Methods

2.1. Neuron models

In this study, we performed simulations for several different neuron models. We designed a novel closed-field layer 1 neurogliaform interneuron model that was parameterized to match patch clamp data, as described in detail below. We also implemented open-field layer 3 and layer 5 pyramidal neuron models [23, 24]. In the final analysis, we simplified the layer 5 pyramidal neuron so it could be scaled to different sizes. These models helped determine the absolute maximum recording depth for common types of neurons in varying layers of the brain and acted as possible sources for the single-unit signals reported in Khodagholy *et al* 2015 [22]. The geometries of all cell models are shown in figure 1.

To consider signals from layer 1 neurons, we built a computational model of a layer 1 neurogliaform neuron of the neocortex based on published layer 1 patch clamp currents [25]. A previous study obtained the morphology of the neuron [26], available at neuromorpho.org. We imported the morphology into the HOC format of the software package, NEURON, using the built-in import3D tool [27]. The model had an active somatic compartment and 45 passive dendritic compartments. We calculated the number of segments in each compartment (nseg) using the d-lambda rule [27]. We then tuned the model parameters to obtain biologically realistic properties. This tuning was done in two stages: we first turned the model's passive properties. We tuned the model's specific membrane resistance (15.4 kΩ cm^2) to match the time constants (15.4 ms) and input resistance (297MΩ) with experimental values [25]. Next, we tuned the model's active properties to match the spike shape characteristics with that of the experimental data. For this purpose, we inserted Hodgkin–Huxley type [28] voltage-gated sodium and delayed rectifier potassium currents into the model's somatic compartment. The transmembrane currents, illustrated in figure 2, are based on a previously-published study that included neurogliaform cells [29] (see the appendix for equations). We tuned the maximal channel conductance (gmax) values of voltage-gated sodium and potassium channels using a brute force search approach and feature based error functions [30, 31]. We then chose the

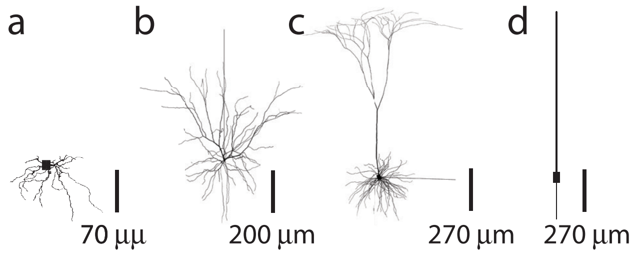

Figure 1. Structure of the NEURON models. (a) Layer 1 neurogliaform interneuron [26] (b) Layer 3 pyramidal cell [24] (c) Layer 5 pyramidal cell [23, 24] (d) Scalable neuron model derived from layer 5 pyramidal neuron.

features: spike width, spike threshold, spike amplitude and after-hyperpolarization amplitude. By assuming parameter specific maximum values, we evaluated the error function at equidistant points in the parameter space [30]. The resulting model (Na gmax = 2 S cm^{-2}, K gmax = 0.3 S cm^{-2}) had a spike threshold of −49.4 mV and a spike width of 0.805 ms closely replicating the spike shape of experimentally-measured neurogliaform neurons. The model's spike amplitude was 44% larger than that of experimental data [25]. We performed all simulations at 32 °C. To model the temperature dependence of the ionic currents, we employed a q10 value of 3 to scale the gating time constants of channel currents. The model had a resting membrane potential of −82.36 mV.

We also included well-established models of layers 3 and layer 5 open-field pyramidal cells [23, 24]. We only considered open-field pyramidal neurons because their long and thick apical dendrites can lead to significant spatial separation between sources or sinks and the corresponding return currents that produce significant ionic currents in the extracellular space [32]. We reasoned these open-field neurons would produce spikes that would be most likely to appear in extracellular recordings from electrodes at distant locations.

Finally, we created a simplified version of the layer 5 pyramidal neuron from Mainen *et al* 1995 [23] to scale the neuron size with all other parameters held constant [23, 33]. This allowed us to explore potential difficulties when recording from small neurons with most surface and penetrating electrodes. We kept the channel types, channel dynamics, and overall ion channel counts within each part of the cell consistent with the Mainen model. However, we simplified the overall neuron geometry. The axon was shortened to a single myelinated 200-compartment section with a length of 100 μm and a diameter of 1 μm since the axon makes a small contribution to the extracellular action potential [34, 35]. The axon hillock compartments were kept the same with the diameters increasing from 1 to 9 μm approaching the soma. For the soma, the cylindrical compartment was set to a diameter of 24 μm and height of 21 μm to match the neuron size used in the original layer 5 model [23, 36]. Finally, we consolidated the elaborate dendritic arbor in Mainen *et al* 1995 [23] into a single thick dendrite with 222 segments, length of 1030 μm, and a diameter of 12 μm. While the length of the apical dendrite compartment remained approximately the same, we increased the diameter so that the total surface area matched that of the original dendritic arbor (65 000 μm^2) [34, 37]. In all regions of the cell, we calculated the channel density such that the overall density of ion channels in each section of the neuron remained the same as the original model from Mainen *et al* 1995 [23]. When altering the neuron size, we linearly scaled the entire model geometry to match the soma diameter of the neuron in question.

Table 1. Electrical and dimensional properties for finite element analysis. Electrical conductivities were attained from previous modeling studies [11, 39, 49, 64].

Domain	Conductivity (S m^{-1})	Radius/Size (μm)
Brain (Grey matter)	0.333	8000
Cerebrospinal fluid	1.7857	8500
Skull	6.25×10^{-3}	9000
Scalp	0.434 78	10 000
PEDOT:PSS	96 000	$10 \times 10 \times 10$ μm^3
GOLD	4.56×10^7	$10 \times 10 \times 8$ μm^3
Parylene	1.6667×10^{-15}	2 μm (thickness)

We performed all simulations within the NEURON 7.2 simulation environment. To generate action potentials in the layer 1, 3, and 5 pyramidal cell models, we injected current into the soma. To generate action potentials in the simplified pyramidal cell model, we injected a brief pulse of current into the axon hillock at the minimum current which would cause an action potential (pulse width = 7 ms, pulse amplitude = 0.7 nA for a 24 μm diameter neuron). For each neuron model, we solved the time-dependent transmembrane currents in each compartment.

2.2. Volume conductor model

To evaluate the effects of electrode size, position, and insulation, we created finite element models (FEM) of a rat brain and μECoG electrodes. Similarly to Moffitt and McIntyre, 2005 [11] this model included rodent head dimensions with representations of the brain, cerebrospinal fluid (CSF), skull, and scalp as shown in table 1. We implemented an electrostatic model with the above dimensions in COMSOL 5.2a (Comsol Inc., Burlington Massachusetts). When the mesh spacing was reduced 2 fold, the mean squared error between the two solutions was 0.0107 μV. Thus, the mesh was determined stable. For computational simplicity, we flattened the top of the brain, forming a circle with a diameter of 1130 μm. Although μECoG electrodes traditionally sit on top of the pia, we assumed the pia to have a conductivity equal to the brain since the pia exerts a negligible difference on field potential distribution [38–40].

The microelectrodes within this model were based on the electrodes described in Khodagholy *et al* 2011 [41] and Khodagholy *et al* 2015 [22]. The electrode consisted of a $10 \times 10 \times 8$ μm^3 volume of gold surrounded by a $10 \times 10 \times 10$ μm^3 cube of PEDOT:PSS backed by a 2 μm thick layer of parylene-c insulation extending for 50 μm past the electrode on either side, meant to simulate full insulation coverage (figure 3). For comparison a single, more accurate, representation of the electrode was created with $10 \times 10 \times 1.79$ μm^3 of a

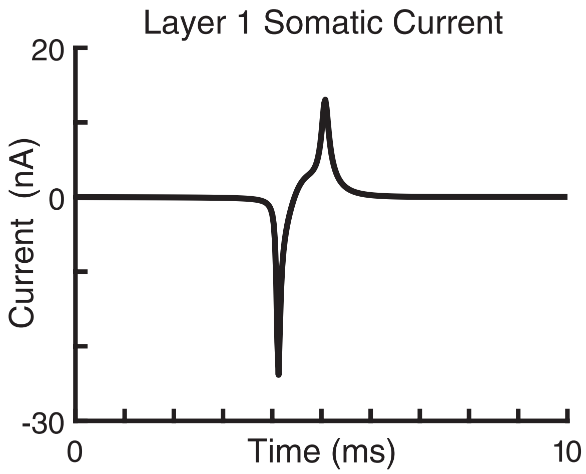

Figure 2. Layer 1 neurogliaform cell transmembrane currents. The somatic current had a 24 nA trough followed by a sharp 13 nA peak.

PEDOT:PSS/Ethylene Glycol mix on top of a $10 \times 10 \times 0.21$ μm^3 solid gold electrode backed by a $150 \times 150 \times 2$ μm^3 parylene-c substrate with parylene-c, 2 μm thick, surrounding the electrode laterally. A difference of less than 1% was observed between the two models. The electrode contact was placed at the top of the brain with the skull acting as the ground. The electrical conductivities for each material are listed in table 1. We also created variants of this electrode with different contact sizes and width of lateral insulation.

To achieve a model solution, we applied the necessary load and boundary conditions. The load condition consisted of a unit current source (i.e. 1 A) placed at the recording electrode [11, 39, 42]. The boundary conditions required that the voltage attenuated to zero at the skull. The electrostatic model was solved in COMSOL using a linear solver.

2.3. Waveform calculation

To estimate the neural spike waveforms recorded from a particular electrode and neuron, we used a reciprocal solution [11, 42] to couple the volume conductor FEM to the neuron models. Each compartment of a neuron model was represented as an independent current source (i.e. the time-dependent transmembrane currents computed in NEURON) at the appropriate spatial location in the FEM. We then calculated the recorded waveform by summing the voltages generated at the electrode contact by each of the transmembrane currents of the individual neuron compartments. Briefly, the reciprocal solution involved placing a unit current source at the recording electrode and solving for the scalar potentials generated at each node in the FEM. By the theorem of reciprocity, the voltage at a given node in the mesh could be interpreted as the voltage generated at the recording electrode for a unit current. Therefore, we calculated the contribution of each neural compartment to the recorded waveform using interpolation of the voltages from the nearest nodes surrounding each neural compartment. See Moffitt and McIntyre, 2005 [11] and Lempka *et al*, 2011 [42] for additional details describing this reciprocal solution approach.

2.4. Cortical layer imaging

We performed immunohistochemistry to estimate the average diameter, surface area, and density of neural somata in layer 1 of mammalian cortex as well as the thickness of layer 1. We performed all animal procedures in accordance with the institutional animal guidelines and approval of the University of Michigan IACUC. For histology, we perfused WT Long-Evans wild-type rats under anesthesia first with cold saline followed by 10% Neural Buffer Formalin (NBF, Millipore). We removed brains which were postfixed for 16 hours in fresh 10% NBF with gentle shaking at 4 °C. Next, we mounted sections in 2% agarose gel (ThermoFisher) in homemade 1X Phosphate Buffer Saline (PBS) and cut at 100 μm thickness using a Leica VT1000S vibratome. Then, we blocked sections in StartingBlock-PBS (ThermoFisher) with 1.0% Triton X-100 overnight at 4 °C with gentle shaking. We incubated section in mouse anti-neuronal nuclei (NeuN) primary antibody (1:250, Millipore) in PBS containing 0.5% Triton X-100 for 3 d at 4 °C with gentle shaking [43]. We then incubated sections for 2 d in donkey anti-mouse Alexa Fluor 647 (1:500, Jackson ImmunoResearch) and NeuroTrace 435/455 (1:250, Life Technologies) in PBS with 0.5% TritonX-100. We washed sections three times between each incubation using PBS with 0.5% Triton X-100 for one hour each at room temperature. We mounted sections in Vectashield mounting medium (Vector Labs). Finally, we imaged sections at 1 μm intervals in the z-dimension on a Zeiss LSM 780 using 405 nm and 633 nm lasers for excitation together with −405 and 488/543/633 dichroic mirrors.

2.5. Density and morphology of neurons in upper layers

From the histology images described in section 2.4, we observed 718 ± 30.4 neurons per plane with an average radius of 4.59 ± 1.40 μm ($n = 53, 106$) over all cortical layers. Due to the small plane thickness, we counted individual neurons multiple times. We then modeled the neurons as spheres and the center of each neuron was determined using Fiji/ImageJ v1.48 [44, 45]. If the center was within 2 μm on subsequent planes, we considered the neurons to be one neuron captured by multiple planes. Once we removed these duplicated neurons there were a total of 17 901 neurons with an average radius of 4.98 ± 1.60 μm and 344 ± 220 μm^2 surface area over all cortical layers. As seen in figure 4 we separated the layers of cortex and calculated the neuron density, neuron radius, and layer thickness. Average neuron size informed the size of our neuron model for layer 1 neurons. We identified each layer by the neuron density and morphology with pia containing no neurons and having a lighter appearance, layer 1 containing sparse neurons, layer 2/3 increasing drastically in density, layer 4 neurons increasing in soma size, and layer 5 neurons decreasing in soma size. These distinctions, as well as a single optical section of brain, can be seen in figure 4. The depth of the pia (20.2 ± 1.58 μm) set a minimum distance between the electrode and a neuron since neurons do not typically exist in the pia. Since the pia was removed from the rat brain during processing, mouse slices stained with NeuN were used from another study. The depth of the other layers indicated at what depth a large change in neuron density would occur as well as the type of neuron that may be recorded at specific recording depths.

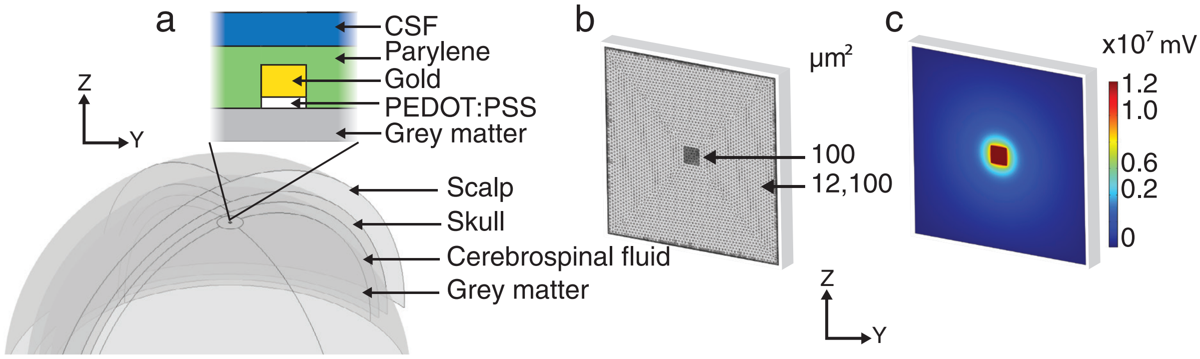

Figure 3. Volume conductor model. (a) The finite element model of the rat head consisted of four spheres (grey matter, CSF, skull, and scalp) and the recording microelectrode described in table 1. (b) Finite element mesh in which the node density was increased dramatically over the electrode and the immediately surrounding area using an adaptive physics controlled mesh defined in Comsol 5.2. C) Voltage distribution generated at the electrode and surrounding tissue from the 1 A current source.

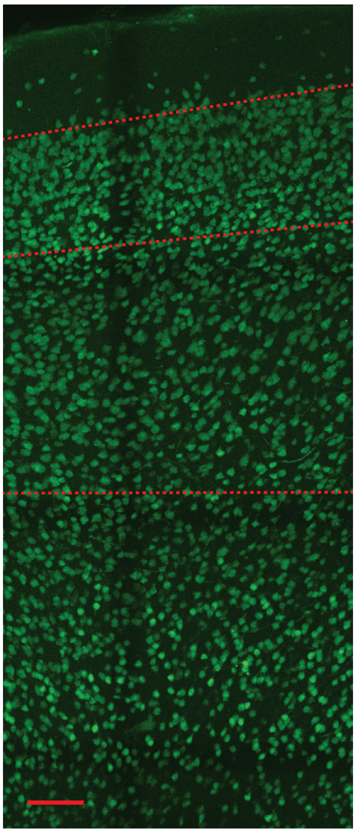

	Density neurons/mm^3	Radius (std) µm
Layer 1	9,830	3.76 (1.04)
Layer 2/3	355,000	5.31 (1.79)
Layer 4	213,000	5.06 (1.60)
Layer 5	198,000	4.77 (1.37)

Figure 4. Rodent brain histological section. One of 73 NeuN-stained coronal sections of cortex. The density of neurons in each layer is indicated in neurons per volume and was calculated over at least 0.005 42 mm^3. The cortical layer thickness was confirmed by Buzsaki *et al* 1998 [40] and Belgard *et al* 2011 [41]. The radius of neurons in each layer were significantly different than each other (layer 1 and layer 5 $p < 0.05$; layer 2/3 and layer 4 $p < 0.001$). Scale bar = 100 μm.

3. Results

3.1. Replication of experimental recordings

First, we used our model to simulate spikes that could potentially be recorded from multiple layers of the brain using an electrode resembling the μECoG arrays used in Khodagholy *et al* 2015 [22]. This electrode was 10×10 μm^2, with 110×110 μm^2 of parylene immediately adjacent to the pia with no CSF between the electrode and the pia, as shown in figure 3. These parameters represent a favorable recording environment, assuming perfect electrode adhesion to tissue. Using the models described above for layer 1, layer 3, and layer 5 neurons, we simulated the resulting spike waveforms on the electrodes and measured the peak-to-peak amplitudes. Recorded waveforms for the cells in each layer are shown across the top of figure 5.

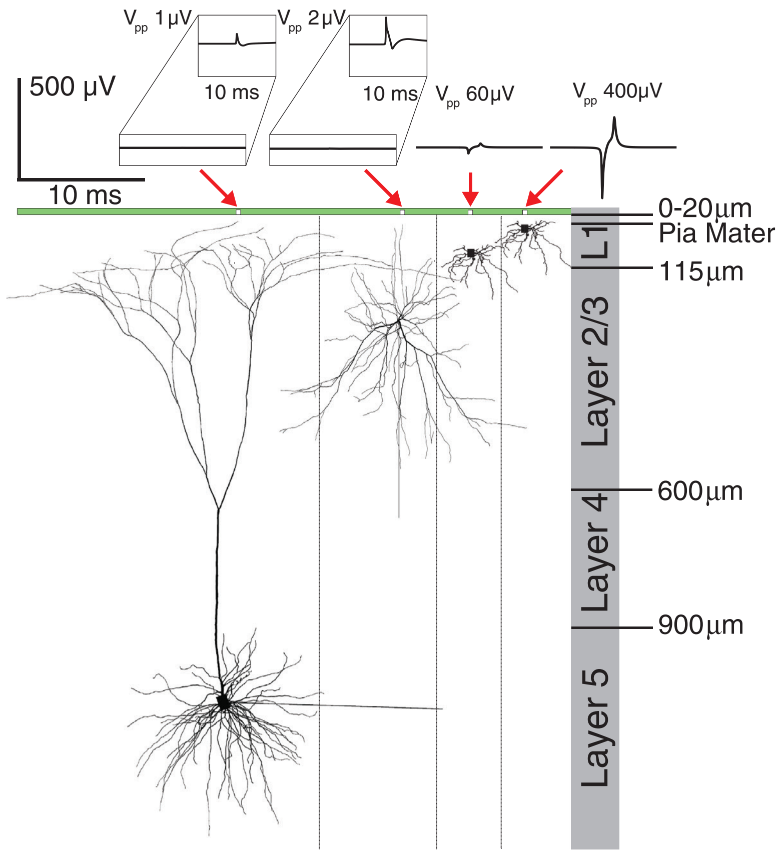

Figure 5. Diagram of various neuron sizes, depths, and recorded spiking activity. According to their respective layers, we placed the layer 1, 3, and 5 model neurons at various distances away from the 100 μm^2 electrode contacts. To provide the optimal recording situation, we placed each neuron on the shallow end of their respective layer while preventing the neuron from extending past the edge of the brain. Axonal and dendritic recordings of layer 3 and 5 neurons never exceeded 1 μV when the neuron was placed at the correct biological depth.

The only simulation that produced a detectable spike (>48 μV_{pp}) was a layer 1 cell placed at the very top of pia, 20 μm away from the recording electrode. If we assume a minimum signal-to-noise ratio (SNR) of 2 to reliably detect a spike and a 12 μV recording noise for a 100 μm^2 electrode [42], then the smallest detectable neuronal spike is ~48 μV (i.e. $V_{\min} = SNR \times 2 \times \sigma_{\text{noise}}$). While the layer 1 neuron spike was very large at 20 μm (400 μV, larger than seen in Khodagholy *et al* 2015), it dropped to 50 μV at only 60 μm away from the electrode. The large V_{pp} at an electrode-to-neuron distance of 20 μm may be attributable to perfect soma positioning and lack of any CSF at the electrode site (modeled below). Models of neurons from layers 3 and 5 only produced very small spikes at the brain surface with rising edge first. In all cases, the amplitude was below 1 μV. Therefore, we focused on layer 1 neurons for the remaining analyses in this study.

Layer 1 cell recording could also reproduce how neurons in Khodagholy *et al* 2015 [22] appear on a single contact or adjacent contacts with detectable amplitudes, but rarely on any distant contacts. Figure 6 shows the waveform amplitude from a simulated layer 1 neuron 20 μm away. It had a peak-to-peak amplitude of 400 μV on the closest contact, a detectable amplitude of 60 μV on the adjacent contact, with 30 μm between the 10×10 μm^2 electrodes, and an amplitude of 4.5 μV two contacts away. The model shows that a neuron placed 30 μm deep, directly between two contacts, produces an amplitude of 135 μV on each contact. If we assume a maximum recording depth of 60 μm, we would be able to record activity from ~20 neurons under a 160×320 μm electrode grid (NeuroGrid) based on the layer 1 thickness and neuron density (9830 neurons mm^3) estimated from our histology results.

Our computational model posited the ideal scenario for recording in which the largest factors affecting the accuracy of this estimate were electrode adhesion to the brain and neuron size. With the addition of a few microns of CSF between the electrode and the brain, the signal decreased by approximately 50%. With CSF present, the estimate of the number of recordable neurons decreased from 20 to 4 neurons. These estimates included 20 μm of pia between the electrode and layer 1 yet other studies indicate that pia is slightly thicker in rats (~25 μm; [46]). If the thickness of pia in rats was increased to 30 μm, then the estimate of the number of recordable neurons decreased from 20 to 15 neurons. The theoretical estimate agreed well with experimental data in which the activity of ~9 individual neurons was consistently detected with the NeuroGrid [22].

3.2. *Effects of electrode geometry, insulation, and adhesion*

After validating the model against experimental results, we explored the design space of electrodes capable of recording

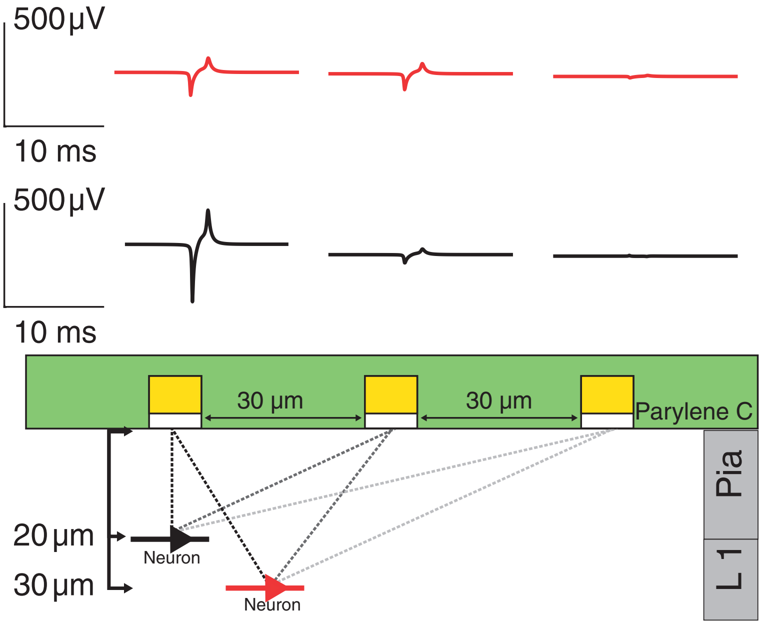

Figure 6. Diagram of simulated μECoG neural recordings. Grid of three 100 μm^2 electrodes on the surface of the brain with a layer 1 neurons at 20 μm deep and 30 μm deep. Inter electrode spacing of 30 μm with insulation (parylene-c) surrounding the electrodes horizontally including a 4 μm layer of insulation on the back.

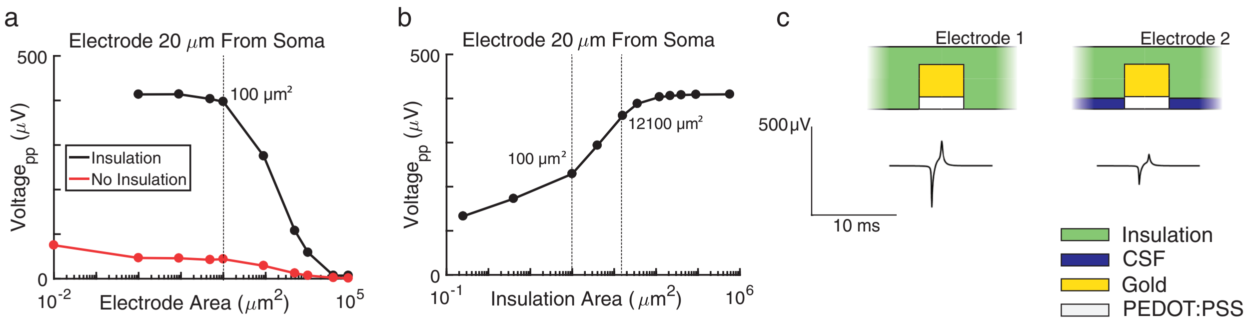

Figure 7. Electrode surface area and insulation's effect on recording amplitude. The recordings originate from a layer 1 neuron 20 μm away from the electrodes. (a) The black traces were recorded using a model with effectively an infinite amount of insulation on the four sides of the electrode and 2 μm of insulation on the back of the electrode. The red traces were recorded using a model with no insulation on the electrodes. The electrodes' surface areas are: 0 μm^2 (10^2 represents a perfect electrode), 1 μm^2, 9 μm^2, 50 μm^2, 100 μm^2, 900 μm^2, 5000 μm^2, 10 000 μm^2, 40 000 μm^2, 90 000 μm^2. (b) The amount of lateral insulation was varied on a 10×10 μm^2 electrode, evaluated at .25 μm^2, 4 μm^2, 100 μm^2, 400 μm^2, 1600 μm^2, 3600 μm^2, 12 100 μm^2, 22 500 μm^2, 40 000 μm^2, 90 000 μm^2, 577 600 μm^2. (c) A comparison between the ideal model, where the electrode is perfectly adhered to the brain, and a more realistic recording environment, where 3.5 μm of insulation was replaced with highly conductive CSF. The thin layer of CSF decreases the signal amplitude by 55%.

surface single units in terms of size, insulation, and adhesion. Electrode surface area is a critical design parameter, with site sizes of 100 μm^2 or smaller requiring highly conductive surface preparations and microfabrication due to their high impedance [22, 47]. Figure 7(a) shows the recording amplitude as a function of electrode surface area for a layer 1 neuron 20 μm from the electrode. The recording amplitude rapidly decreases for electrode surface areas larger than 100 μm^2, which suggests electrodes should have surface areas = 100 μm^2 to detect single-unit activity from the brain surface. Therefore, previous μECoG electrodes may not have been small enough to detect single units.

Insulation was also critical for high recording amplitudes in the model. Electrodes without insulation (i.e. parylene replaced with CSF) produced low recording amplitudes (figure 7(a)). Therefore, we also varied the amount of insulation on the back of the electrodes as shown in figure 7(b). To maintain 95% of the signal amplitude, 60×60 μm^2 lateral insulation was required for a 10×10 μm^{-2} recording electrode surface area.

Blood flow and respiration can cause micromovements of the brain where the brain may move vertically up to 4 μm and 30 μm, respectively [48]. To model the effect of these micromovements, as well as electrode adhesion in general, we added a layer of CSF between the insulation and the brain as shown in figure 7(c). We tested CSF thicknesses of 3.5 μm and 30 μm that reduced the recording amplitude by 55% and 97%, respectively. This result suggests that that adhesion is also critical for high amplitude recording.

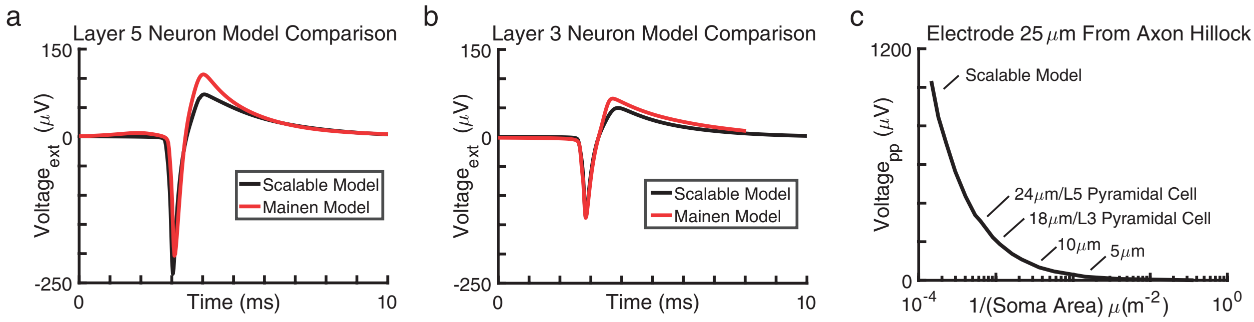

Figure 8. Scalable model validation and neuron size as it relates to voltage spike amplitude. The voltage trace of the scalable pyramidal neuron model compared to the layer 5 (a) and layer 3 (b) pyramidal neuron models [23, 24]. The scalable neuron was scaled to match the approximate soma size of both existing neuron models. The V_{pp} was within 1% of the layer 5 model and 13% of the layer 3 model. (c) Voltage spike amplitude decreased approximately linearly with the surface area of the soma, but can be more accurately modeled as $V_{pp} = 0.6320 \times exp(-0.8366 \times \ln[somaArea^{-1}])$. The layer 5 pyramidal model, the layer 3 pyramidal model, and specific neuron sizes from the scalable model are indicated on the graph.

3.3. Effects of neuron size and channel density

The results above suggest that there can be non-obvious interactions between cell size, distance, and that electrode design choices may significantly impact recording sensitivity. While the distance relationship is well understood [11], we sought to model the effect of neuron size, independent of other parameters. As described in section 2.1, we created a simplified neuron model based on the well-established layer 5 model [23, 24]. Our simplified model used a line of cylinders with equivalent ion channel densities. When we scaled the reduced model to have a soma diameter equal to the diameters of the more detailed models (18 μm for layer 3, 24 μm for layer 5), the spike amplitudes of the reduced model were within 13.3 and 1.0 percent of the spike amplitudes of the layer 3 and layer 5 cell models, respectively (figures 8(a) and (b)). Figure 8(c) shows the effect of scaling the neuron size on voltage amplitude. Overall, if channel densities and properties remain constant as the size of the neuron increases, waveform amplitude scales with soma diameter squared, or equivalently the waveform amplitude scales linearly with soma surface area. This trend is observed because the number of ion channels, and thus the transmembrane current, are scaling with the area in our simplified model and the voltage is linearly proportional to the transmembrane current. In this model, a neuron with a 10 μm diameter would produce a peak-to-peak spike amplitude of 66.8 μV (compared to 307 μV for the 24 μm layer 5 cell), an 8 μm diameter neuron would produce a spike amplitude of 46.0 μV (our estimated minimum detectable signal), and a 5 μm diameter neuron would produce a spike amplitude of 18.5 μV. We altered the density of Na^+ and K^+ ion channels in the simplified neuron by $\pm$50% to determine if these results are sensitive to the specific channel density chosen. The largest signal increase was 7.8% and occurred when the Na^+ channel density was increased and the K^+ channel density was decreased. The largest signal decrease was -1.8% and occurred when the Na^+ channel density was decreased and the K^+ channel density was increased.

4. Discussion

In this modeling study, we explored possible sources of single-unit recordings from μECoG electrodes and examined how future electrode designs can take advantage of this remarkable capability. Towards this end, we used three neuron models: a layer 1 neurogliaform cell, a layer 5 pyramidal cell, and a layer 3 pyramidal cell [23, 24]. We also created a novel neuron model, based on a simplification of a layer 5 pyramidal cell, which could be scaled to illustrate the relationship between neuron size and V_{pp} [23, 24]. We then developed a volume conductor model of the rat head along with various μECoG electrode designs to determine the effect of electrode size and insulation geometry on V_{pp} [11, 39, 49]. The results of our model analyses agreed well with experimental recordings from the literature [22] and predicted the effects of electrode design (e.g. the effect of electrode contact size and insulation geometry) on extracellular recording amplitude.

Specifically, a naive application of a 10×10 μm^2 electrode and a layer 1 neurogliaform cell appeared to accurately replicate the experimental results in Khodagholy *et al* 2015 [22]. Although we recorded a signal from layer 3 and 5 pyramidal neurons in a noise-free environment, the V_{pp} were less than 1 μV. While dendritic currents in aggregate may contribute to low-frequency local field potentials [50, 51], this model suggests dendrites originating from a single neuron are not the source of observed spikes on the surface of the cortex. Furthermore, the density of neuron cell bodies in layer 1 match the density of recorded spikes in Khodagholy *et al* 2015 [22], indicating that the single-unit recordings in Khodagholy *et al* 2015 likely originate from layer 1 neurons.

In this study, we developed a scalable neuron model that allowed us to examine how V_{pp} scaled with neuron size. Our results suggest V_{pp} decayed rapidly with decreasing cell size and cells smaller than 8 μm would be difficult to detect with recording electrodes even at very close distances (figure 8). The difficulty of recording from neurons smaller than 8 μm in diameter is consistent with experimental data showing the challenges of recording from areas with predominantly small neurons, such as songbird areas and dorsal striatum [52, 53].

This result further highlights that single-unit recordings, particularly those from electrodes with large recording surfaces, have been biased toward recording signals from large neurons.

Using the base electrode model developed in this study, we made changes to the surface area of the electrode and the size of the lateral insulation. We determined that increasing the size of the electrode decreased the recording amplitude. The decrease in measured voltage when increasing the surface area of the electrode is expected due to spatial averaging of the voltage over a larger surface area [11, 21, 54, 55]. Furthermore, our model showed a rapid decrease in recording amplitude for electrodes larger than 100 μm^2 (figure 7(a)), indicating that an electrode surface area = 100 μm^2 may be an ideal size for μECoG arrays. The amount of lateral insulation also significantly affected the recording amplitude. For electrodes with no lateral insulation, recording amplitudes were small and would likely be undetectable (figure 7(a)). However, with 3600 μm^2 of lateral insulation, the recording amplitude was 95% of the signal amplitude for a 10×10 μm^2 electrode contact with an effectively infinite amount of lateral insulation. μECoG arrays with this amount of lateral insulation have been fabricated previously [41, 56]. Since the changes to the model are independent, the effects of electrode geometry, insulation, and adhesion, as well as the effects of neuron size and channel density, can be combined using superposition. These results suggest that although μECoG electrode contact dimensions should shrink to the cellular level, the insulation needs to remain fairly large in comparison.

In our model analysis, we also considered the effects of micromovements related to blood flow and respiration that could occur due to non-ideal adhesion between the brain and the electrode. We represented these micromovements using an additional layer of CSF with a variable thickness. This CSF layer substantially decreased the recording amplitude (i.e. 55% and 97% for CSF layers of 3.5 μm and 30 μm, respectively). This is due to the decreased resistance between the electrode and the neurons as well as the low resistance pathway to ground that the CSF provides [11]. This result suggests that adhesion is critical for high-amplitude recordings. Although the adhesion of μECoG electrode arrays to the brain has not been fully investigated, it has been shown that electrode arrays thinner than 5 μm conform well [22, 56]. Further, adhesion and flexibility of μECoG electrode arrays continue to increase through the addition of holes to the substrate and a decrease in array thickness [56].

It is important to note that neurons needed to be within 60 μm of the recording contact to obtain a signal over 50 μV. This short distance raises the question of whether or not these electrodes could function under chronic recording conditions in which they would be surrounded by encapsulation tissue. Previous modeling studies have shown that an increase in tissue resistance due to electrode encapsulation may actually increase the recording amplitude [11, 57]. However, experimental results suggest that ECoG electrodes can develop thick scars ($\sim$1–2 mm) [19] that would likely increase the distance between the electrode and the neurons and produce a corresponding decrease in the recording amplitude. It could be possible to use electrode arrays with elements less than 15 μm in diameter to mitigate scarring [58]. At 10×10 μm^2 the electrode would be small enough to reduce scar formation, but the necessary insulation ($\geqslant$3600 μm^2) would cause scarring when chronically implanted. Thus, biocompatible coatings may be needed for chronically viable electrodes (e.g. Azemi *et al* 2008 [12] and Jorfi *et al* 2015 [14]).

Although this study provided a means to systematically analyze the origin of single-unit surface recordings with μECoG electrodes and the effects of electrode design, our model infrastructure was subject to a number of limitations. First, we made the standard assumption that the electrical properties of the biological media were resistive and linear within the context of neural recording [59]. Model solutions were static and did not consider the resistive and capacitive properties of the electrode-electrolyte interface of the recording electrodes. However, for well-designed recording systems, the electrode-electrolyte interface has a minimal effect on the recorded signal [55, 60–62]. Second, the rat brain anatomy was simplified and represented by four concentric spheres. However, previous work has shown that computer models of extracellular microelectrode recordings are largely insensitive to the geometry of the head model [11, 39]. Third, because we only considered acute neural recordings in this study, we did not investigate the effects of electrode encapsulation and the corresponding changes in tissue impedance surrounding the electrode that could potentially affect the recording amplitude for a given electrode design [11, 57]. Fourth, in the simplified layer 5 pyramidal neuron model, we collapsed the dendritic arbor into one large apical dendrite which increases the length constant of the neuron. This increase in length constant could make the neuron electronically compact and produce a small increase in the amplitude of the extracellular action potential [34, 37]. Fifth, although the simulated layer 1 neuron came from a validated study, it is larger than the average layer 1 neuron. When the neuron model spike size was matched artificially, the spike size decreased by 56%. Finally, we did not incorporate noise sources (e.g. thermal, biological) into our model analysis. Recording noise sources, such as thermal noise, could play a significant role in determining the optimal contact size since these noise sources can vary with contact size [42, 63].

5. Conclusion

In this study, we used a computational model of neural recording with μECoG electrodes to investigate the ability to record individual neurons from the surface of the brain and determine the design parameters that support single-unit recording. Our modeling results corroborated experimental data demonstrating single-unit recordings with μECoG electrodes. Our results also suggested that these signals most likely originate from layer 1 of cortex [22]. It is important to note that the recording amplitude, and consequently the recording depth, depend heavily upon the adhesion of the electrode to the brain. Although μECoG electrodes cannot record from deep layer neurons, many applications that consistently utilize interneurons in superficial layers of the brain, such as epilepsy, would benefit from recording that activity of superficial neural signals [1, 20]. In this study, we also characterized the recording amplitude's dependence on lateral insulation and electrode size. Model results show that both design parameters significantly affected the recording amplitude and these parameters must be considered in future studies. In spite of the challenges, the ability to record individual neurons without penetrating the brain provides new scientific and clinical opportunities that may change how we interact with the brain.

Acknowledgments

The authors would like to thank Jonathan Viventi PhD for insightful comments on this paper. This work was supported by multiple grants from the National Institute of Health: 5R01 MH110932, 3U01 NS094375, and NIH BRAIN Initiative grants 5U01 NS094375-02 and 1R03 MH111316-01. The work was also supported by the National Science Foundation's International Program for the Advancement of Neurotechnology (IPAN), the American Epilepsy Society Junior Investigator Award, and a miBRAIN grant.

Appendix. Equations for layer 1 neuron ion channel currents

A.1. Fast sodium current

$$\alpha_m = -0.034\,133 \times \frac{\nu + 24}{exp(\frac{\nu+24}{-5}) - 1} \tag{A.1}$$

$$\beta_m = 0.2848 \times \frac{\nu - 4}{exp(\frac{\nu-4}{5}) - 1} \tag{A.2}$$

$$\tau_m = \frac{1}{\alpha_m + \beta_m} \tag{A.3}$$

$$m_\infty = \frac{\alpha_m}{\alpha_m + \beta_m} \tag{A.4}$$

$$\alpha_h = \frac{0.296\,48}{exp(\frac{\nu+64.4184}{20})} \tag{A.5}$$

$$\beta_h = \frac{3.0931}{1 + exp(\frac{\nu+12.1463}{-10})} \tag{A.6}$$

$$\tau_h = \frac{1}{\alpha_h + \beta_h} \tag{A.7}$$

$$h_\infty = \frac{\alpha_h}{\alpha_h + \beta_h} \tag{A.8}$$

$$I_{Na} = gmax \times m^3 \times h \times (V - E_{Na}). \tag{A.9}$$

A.2. Delayed rectifier potassium current

$$\alpha_n = -0.07 \times \frac{\nu + 8}{exp(\frac{\nu+8}{-6}) - 1} \tag{A.10}$$

$$\beta_n = 0.264 \times exp(\frac{\nu + 33}{40}) \tag{A.11}$$

$$\tau_n = \frac{1}{\alpha_n + \beta_n} \tag{A.12}$$

$$n_\infty = \frac{\alpha_n}{\alpha_n + \beta_n} \tag{A.13}$$

$$I_K = gmax \times m^4 \times (V - E_K). \tag{A.14}$$

ORCID iDs

Mackenna Hill https://orcid.org/0000-0003-4417-3723

References

[1] Viventi J *et al* 2011 Flexible, foldable, actively multiplexed, high-density electrode array for mapping brain activity *in vivo Nat. Neurosci.* **14** 1599–605

[2] Wray C D *et al* 2012 Multimodality Localization of the Sensorimotor Cortex in Pediatric Patients Undergoing Epilepsy Surgery *J. Neurosurg. Pediatr.* **10**

[3] Rosin B, Slovik M, Mitelman R, Rivlin-Etzion M, Haber S N, Israel Z, Vaadia E and Bergman H 2011 Closed-loop deep brain stimulation is superior in ameliorating parkinsonism *Neuron* **72** 370–84

[4] Schwartz A B 2004 Cortical neural prosthetics *Annu. Rev. Neurosci.* **27** 487–507

[5] Moxon K A and Foffani G 2015 Brain-machine interfaces beyond neuroprosthetics *Neuron* **86** 55–67

[6] Schroeder K E and Chestek C A 2016 Intracortical brain-machine interfaces advance sensorimotor neuroscience *Frontiers Neurosci.* **10** 1–8

[7] Nordhausen C T, Rousche P J and Normann R A 1994 Optimizing recording capabilities of the Utah intracortical electrode array *Brain Res.* **637** 27–36

[8] Yoon T H, Hwang E J, Shin D Y, Park S I, Oh S J, Jung S C, Shin H C and Kim S J 2000 A micromachined silicon depth probe for multichannel neural recording *IEEE Trans. Biomed. Eng.* **47** 1082–7

[9] Vetter R J, Williams J C, Hetke J F, Nunamaker E A and Kipke D R 2004 Chronic neural recording using silicon-substrate microelectrode arrays implanted in cerebral cortex *IEEE Trans. Biomed. Eng.* **51** 896–904

[10] Biran R, Martin D C and Tresco P A 2005 Neuronal cell loss accompanies the brain tissue response to chronically implanted silicon microelectrode arrays *Exp. Neurol.* **195** 115–26

[11] Moffitt M A and McIntyre C C 2005 Model-based analysis of cortical recording with silicon microelectrodes *Clin. Neurophysiol.* **116** 2240–50

[12] Azemi E, Stauffer W R, Gostock M S, Lagenaur C F and Cui X T 2008 Surface immobilization of neural adhesion molecule L1 for improving the biocompatibility of chronic neural probes: *in vitro* characterization *Acta Biomater.* **4** 1208–17

[13] Barrese J C, Rao N, Paroo K, Triebwasser C, Vargas-Irwin C, Franquemont L and Donoghue J P 2013 Failure mode analysis of silicon-based intracortical microelectrode arrays in non-human primates *J. Neural Eng.* **10** 066014

[14] Jorfi M, Skousen J L, Weder C and Capadona J R 2015 Progress towards biocompatible intracortical microelectrodes for neural interfacing applications *J. Neural Eng.* **12** 011001

[15] Patel P R, Zhang H, Robbins M T, Nofar J B, Marshall S P, Kobylarek M J, Kozai T D Y, Kotov N A and Chestek C A 2016 Chronic *in vivo* stability assessment of carbon fiber microelectrode arrays *J. Neural Eng.* **13** 066002
[16] Luan L *et al* 2017 Ultraflexible nanoelectronic probes form reliable, glial scar-free neural integration *Sci. Adv.* **3** e1601966
[17] Skousen J L, Merriam S M E, Srivannavit O, Perlin G, Wise K D and Tresco P A 2011 Reducing surface area while maintaining implant penetrating profile lowers the brain foreign body response to chronically implanted planar silicon microelectrode arrays *Progress in Brain Research* vol 194, 1st edn, ed M G J Schouenborg and N Danielsen ch 12, pp 167–80
[18] Nguyen J K, Park D J, Skousen J L, Hess-Dunning A E, Tyler D J, Rowan S J, Weder C and Capadona J R 2014 Mechanically-compliant intracortical implants reduce the neuroinflammatory response *J. Neural Eng.* **11** 056014
[19] Degenhart A D *et al* 2016 Histological evaluation of a chronically implanted electrocorticographic electrode grid in a non-human primate *J. Neural Eng.* **13** 046019
[20] Solovey G, Miller K J, Ojemann J G, Magnasco M O and Cecchi G A 2012 Self-regulated dynamical criticality in human ECoG *Frontiers Integr. Neurosci.* **6** 44
[21] Holt G R and Koch C 1999 Electrical interactions via the extracellular potential near cell bodies *J. Comput. Neurosci.* **6** 169–84
[22] Khodagholy D, Gelinas J N, Thesen T, Doyle W, Malliaras G G and Buzsáki G 2015 NeuroGrid: recording action potentials from the surface of the brain *Nature Neurosci.* **18** 310–5
[23] Mainen Z F, Joerges J, Huguenard J R and Sejnowski T J 1995 A model of spike initiation in neocortical pyramidal neurons *Neuron* **15** 1427–39
[24] Mainen Z F and Sejnowski T J 1996 Influence of dendritic structure on firing pattern in model neocortical neurons *Nature* **382** 363–6
[25] Cruikshank S J, Ahmed O J, Stevens T R, Patrick S L, Amalia N, Elmaleh M and Connors B W 2012 Thalamic control of layer 1 circuits in prefrontal cortex *J. Neurosci.* **32** 17813–23
[26] Muralidhar S, Wang Y and Markram H 2014 Synaptic and cellular organization of layer 1 of the developing rat somatosensory cortex *Frontiers Neuroanatomy* **7** 1–17
[27] Hines M L and Carnevale N T 2001 NEURON : a tool for neuroscientists *Neuroscientist* **7** 123–35
[28] Hodgkin A L and Huxley A F 1952 A quantitative description of membrane current and its application to conduction and excitation in nerve *Bull. Math. Biol.* **52** 25–71
[29] Bezaire M J, Raikov I, Burk K, Vyas D and Soltesz I 2016 Interneuronal mechanisms of hippocampal theta oscillations in a full-scale model of the rodent CA1 circuit *eLife* **5** 1–106
[30] Prinz A A, Billimoria C P and Marder E 2003 Alternative to hand-tuning conductance-based models: construction and analysis of databases of model neurons *J. Neurophysiol.* **90** 3998–4015
[31] Van Geit W, De Schutter E and Achard P 2008 Automated neuron model optimization techniques: A review *Biol. Cybern.* **99** 241–51
[32] Buzsáki G, Anastassiou C A and Koch C 2012 The origin of extracellular fields and currents–EEG, ECoG, LFP and spikes *Nature Rev. Neurosci.* **13** 407–20
[33] McIntyre C C, Richardson A G and Grill W M 2002 Modeling the excitability of mammalian nerve fibers: influence of afterpotentials on the recovery cycle *J. Neurophysiol.* **87** 995–1006
[34] Gold C, Henze D A, Koch C and Buzsáki G 2006 On the origin of the extracellular action potential waveform: a modeling study on the origin of the extracellular action potential waveform: a modeling study *J. Neurophysiol.* **95** 3113–28
[35] Hay E, Schurmann F, Markram H and Segev I 2013 Preserving axosomatic spiking features despite diverse dendritic morphology *J. Neurophysiol.* **109** 2972–81
[36] Larkman A and Mason A 1990 Correlations between morphology and electrophysiology of pyramidal neurons in slices of rat visual cortex. I. Establishment of cell classes *J. Neurosci.* **10** 1415–28
[37] Rall W, Burke R E, Holmes W R, Jack J J B, Redman S J and Segev I 1992 Matching dendritic neuron models to experimental-data *Physiol. Rev.* **72** S159–86
[38] Sin K 1983 Electrical stimulation of the spinal cord: a further analysis relating to anatomical factors and tissue properties *Med. Biol. Eng. Comput.* **21** 264–9
[39] Slutzky M W, Jordan L R, Krieg T, Chen M, Mogul D J and Miller L E 2010 Optimal spacing of surface electrode arrays for brain machine interface applications *J. Neural Eng.* **7** 26004
[40] Mazzoni A, Lindén H, Cuntz H, Lansner A, Panzeri S and Einevoll G T 2015 Computing the local field potential (LFP) from integrate-and-fire network models *PLoS Comput. Biol.* **11** 1–38
[41] Khodagholy D, Doublet T, Gurfinkel M, Quilichini P, Ismailova E, Leleux P, Herve T, Sanaur S, Bernard C and Malliaras G G 2011 Highly conformable conducting polymer electrodes for *in vivo* recordings *Adv. Mater.* **23** 268–72
[42] Lempka S F, Johnson M D, Moffitt M A, Otto K J, Kipke D R and McIntyre C C 2011 Theoretical analysis of intracortical microelectrode recordings *J. Neural Eng.* **8** 45006
[43] Gittins R and Harrison P J 2004 Neuronal density, size and shape in the human anterior cingulate cortex: a comparison of Nissl and NeuN staining *Brain Res. Bull.* **63** 155–60
[44] Schneider C A, Rasband W S and Eliceiri K W 2012 NIH image to imageJ: 25 years of image analysis *Nat. Methods* **9** 671–5
[45] Schindelin J *et al* 2012 Fiji: an open-source platform for biological-image analysis *Nat. Methods* **9** 676–82
[46] Nowak K, Mix E, Gimsa J, Strauss U, Sriperumbudur K K, Benecke R and Gimsa U 2011 Optimizing a Rodent model of Parkinson's disease for exploring the effects and mechanisms of deep brain stimulation *Parkinson's Dis.* **2011** 1–19
[47] Yoshida Kozai T D, Langhals N B, Patel P R, Deng X, Zhang H, Smith K L, Lahann J, Kotov N A and Kipke D R 2012 Ultrasmall implantable composite microelectrodes with bioactive surfaces for chronic neural interfaces *Nat. Mater.* **11** 1065–73
[48] Gilletti A and Muthuswamy J 2006 Brain micromotion around implants in the rodent somatosensory cortex *J. Neural Eng.* **3** 189–95
[49] Wongsarnpigoon A and Grill W M 2008 Computational modeling of epidural cortical stimulation *J. Neural Eng.* **5** 443–54
[50] Katzner S, Nauhaus I, Benucci A, Bonin V, Ringach D L and Carandini M 2009 Local origin of field potentials in visual cortex *Neuron* **61** 35–41
[51] Pesaran B 2009 Uncovering the mysterious origins of local field potentials *Neuron* **61**
[52] Markowitz J E, Liberti W A, Guitchounts G, Velho T, Lois C and Gardner T J 2015 Mesoscopic patterns of neural activity support songbird cortical sequences *PLoS Biol.* **13** 1–20
[53] Mallet N, Schmidt R, Leventhal D, Chen F, Amer N, Boraud T and Berke J D 2016 Arkypallidal cells send a stop signal to striatum *Neuron* **89** 308–16

[54] Robinson D 1968 The electrical properties of metal microelectrodes *Proc. IEEE* **56** 1065–71

[55] Moulin C, Glière A, Barbier D, Joucla S, Yvert B, Mailley P and Guillemaud R 2006 A new 3D finite element model based on thin film approximation for microelectrode array recording of extracellular action potential *IEEE Trans. Biomed. Eng.* **55** 683–92

[56] Kim D-H *et al* 2010 Dissolvable films of silk fibroin for ultrathin conformal bio-integrated electronics *Nat. Mater.* **9** 511–7

[57] Malaga K A *et al* 2016 Data-driven model comparing the effects of glial scarring and interface interactions on chronic neural recordings in non-human primates *J. Neural Eng.* **13** 16010

[58] Fu T-M, Hong G, Zhou T, Schuhmann T G, Viveros R D and Lieber C M 2016 Stable long-term chronic brain mapping at the single-neuron level *Nat. Methods* **13** 875–82

[59] Plonsey R 1969 *Bioelectric Phenomena* (New York: McGraw-Hill) (https://doi.org/10.1002/047134608X.W1403)

[60] Nelson M J, Pouget P, Nilsen E A, Patten C D and Schall J D 2008 Review of signal distortion through metal microelectrode recording circuits and filters *J. Neurosci. Methods* **169** 141–57

[61] Stacey W C, Kellis S, Patel P R, Greger B and Butson C R 2012 Signal distortion from microelectrodes in clinical EEG acquisition systems *J. Neural Eng.* **9** 056007

[62] Lempka S F and McIntyre C C 2013 Theoretical analysis of the local field potential in deep brain stimulation applications *PLoS One* **8**

[63] Huigen E, Peper A and Grimbergen C A 2002 Investigation into the origin of the noise of surface electrodes *Med. Biol. Eng. Comput.* **40** 332–8

[64] Kim Y H, Sachse C, MacHala M L, May C, Müller-Meskamp L and Leo K 2011 Highly conductive PEDOT:PSS electrode with optimized solvent and thermal post-treatment for ITO-free organic solar cells *Adv. Funct. Mater.* **21** 1076–81